Investigation of combinatorial coevaporated thin film Cu_2ZnSnS_4. I. Temperature effect, crystalline phases, morphology, and photoluminescence

Hui Du,[1,a)] Fei Yan,[1,b)] Matthew Young,[1] Bobby To,[1] Chun-Sheng Jiang,[1] Pat Dippo,[1] Darius Kuciauskas,[1] Zhenhuan Chi,[2] Elizabeth A. Lund,[3] Chris Hancock,[3] Win Maw Hlaing OO,[3] Mike A. Scarpulla,[3] and Glenn Teeter[1,c)]

[1]*National Renewable Energy Laboratory, 15013 Denver West Parkway, MS3218, Golden, Colorado 80401, USA*

[2]*Renishaw Incorporated, 5277 Trillium Blvd., Hoffman Estates, Illinois 60192, USA*

[3]*Departments of Chemical Engineering, Electrical & Computer Engineering, and Materials Science & Engineering, University of Utah, Salt Lake City, Utah 84112, USA*

(Received 29 October 2013; accepted 30 January 2014; published online 2 May 2014)

Cu_2ZnSnS_4 is a promising low-cost, nontoxic, earth-abundant absorber material for thin-film solar cell applications. In this study, combinatorial coevaporation was used to synthesize individual thin-film samples spanning a wide range of compositions at low (325 °C) and high (475 °C) temperatures. Film composition, grain morphology, crystalline-phase and photo-excitation information have been characterized by x-ray fluorescence, scanning electron microscopy, x-ray diffraction, Raman spectroscopy, and photoluminescence imaging and mapping. Highly textured columnar grain morphology is observed for film compositions along the ZnS-Cu_2ZnSnS_4-Cu_2SnS_3 tie line in the quasi-ternary Cu_2S-ZnS-SnS_2 phase system, and this effect is attributed to structural similarity between the Cu_2ZnSnS_4, Cu_2SnS_3, and ZnS crystalline phases. At 475 °C growth temperature, Sn-S phases cannot condense because of their high vapor pressures. As a result, regions that received excess Sn flux during growth produced compositions falling along the ZnS-Cu_2ZnSnS_4-Cu_2SnS_3 tie line. Room-temperature photoluminescence imaging reveals a strong correlation for these samples between film composition and photoluminescence intensity, where film regions with Cu/Sn ratios greater than ~2 show strong photoluminescence intensity, in comparison with much weaker photoluminescence in regions that received excess Sn flux during growth or subsequent processing. The observed photoluminescence quenching in regions that received excess Sn flux is attributed to the effects of Sn-related native point defects in Cu_2ZnSnS_4 on non-radiative recombination processes. Implications for processing and performance of Cu_2ZnSnS_4 solar cells are discussed. © *2014 AIP Publishing LLC*. [http://dx.doi.org/10.1063/1.4871664]

I. INTRODUCTION

$Cu_2ZnSn(S,Se)_4$ (CZTSSe) materials are earth abundant and nontoxic, and have recently attracted significant research interest for thin-film photovoltaic (PV) applications as alternatives to $CuIn_{1-x}Ga_xSe_2$ (CIGS) and CdTe.[1–5] Extensive efforts have been made using both vacuum-based and non-vacuum approaches to synthesis.[6–11] Thus far, the highest device efficiency for CZTSSe, 12.0%, was achieved using a non-vacuum synthesis method based on liquid-phase precursor.[6] On the other hand, a vacuum-based deposition method has yielded 8.4% for pure sulfide Cu_2ZnSnS_4 (CZTS) thin films.[12]

Based on theoretical and experimental results, at thermodynamic equilibrium single-phase CZTS is expected to exist only in a narrow region of the quasi-ternary Cu_2S-ZnS-SnS_2 phase diagram, which consists of binary, ternary, and quaternary phases.[13,14] In addition, film composition is expected to control point-defect concentrations, which play a dominant role in determining critical opto-electronic properties, including doping type and level via donor and acceptor states, minority-carrier lifetimes via deep-level defects, and electron and hole mobilities.[15–18] Conventional approaches for mapping material properties in composition space by sequential synthesis and characterization of individual compositions can be very time consuming, and can miss important factors that affect material properties unless synthesis conditions are highly repeatable. Combinatorial methods, in which an individual sample with well-defined synthesis conditions spans a range of compositions, can be an efficient and effective methodology for identifying trends and correlations between composition, processing conditions, and material properties.[19]

In this study, CZTS thin-film samples covering a wide range of composition ratios were deposited at 325 °C and 475 °C via coevaporation using Cu, Zn, and Sn effusion cells, and a valved-cracking source for sulfur. Film properties are mapped by x-ray fluorescence (XRF), scanning electron microscopy (SEM), x-ray diffraction (XRD), and Raman spectroscopy, and correlations between composition, morphology, and crystalline-phase information are drawn from these data. Favorable film morphologies are observed in a composition zone characterized by Cu/Sn ~ 2 in the

[a)]Present address: Sion Power Corporation, 2900 E Elvira Rd., Tucson, Arizona 86756, USA.

[b)]Present address: Applied Materials Inc., 3101 Scott Blvd., Santa Clara, California 95054, USA.

[c)]Author to whom correspondence should be addressed. Electronic mail: glenn.teeter@nrel.gov

quasi-ternary Cu_2S-ZnS-SnS_2 phase diagram, corresponding to coexistence regions between CZTS and the secondary phases ZnS and Cu_2SnS_3 (CTS), which have very similar unit cells and lattice parameters. We speculate that the common observation that optimal device performance is achieved in films with excess Zn could derive in part from this structural coherency. First-principles theory predicts that excess Zn promotes a beneficial distribution of point defects and point-defect complexes in CZTS.[15,17] In Zn-rich films, the formation of isolated grains of ZnS that do not disrupt overall film morphology or impede current collection might be benign, or even help to passivate grain boundaries.[15,17,18]

II. MATERIALS AND METHODS

CZTS thin films were deposited in a high-vacuum physical vapor deposition system with base pressure of $\sim 10^{-6}$ Torr. Metal fluxes were supplied from effusion cells containing 99.996%-pure Cu, 99.993%-pure Zn, and 99.995%-pure Sn (Alfa-Aesar). Sulfur (99.998%-pure, Alfa-Aesar) was supplied by a valved cracker, operated with a bulk-zone temperature of 451 K to provide a sufficiently high flux of sulfur during growth to produce only sulfide crystalline phases. The sulfur cracking-zone temperature was maintained at 1100 K to maximize the ratio of the highly reactive cracked species, S_2, relative to larger vapor-phase sulfur clusters, as confirmed by residual gas analyzer (RGA) measurements. Metal fluxes were calibrated with a combination of quartz crystal microbalance (QCM) and electron impact emission spectroscopy (EIES) sensors. As illustrated schematically in Fig. 1, the deposition chamber is equipped with translatable combinatorial apertures for each of the metal effusion cells. When inserted, these apertures produce laterally graded fluxes across the substrate, yielding thin-film samples with composition gradients. These combinatorial apertures are oriented at 120° relative to one another. With this configuration, film compositions map approximately into a quasi-ternary phase space with respect to metal compositions. No combinatorial aperture was used for the sulfur source. Based on QCM, EIES, and *ex situ* film-thickness calibrations, the growth rate for the thin-film CZTS samples in this study was typically 2.1 Å/s. CZTS films were deposited on molybdenum-coated soda-lime glass (Mo/SLG) substrates measuring 15 mm $\times$ 20 mm. During growth the substrates were radiatively heated from a molybdenum puck, which in turn is radiatively heated by a ceramic heater. With this arrangement, it is possible to achieve substrate temperatures beyond 600 °C. For this study, substrate temperatures during film growth were maintained either at 325 °C or 475 °C. The temperature set-point was maintained during growth using a type-K thermocouple junction clamped to the sample stage near the molybdenum sample puck, and calibrated in separate runs using a type K thermocouple junction clamped to the face of Mo/SLG substrate. Accuracy for temperature measurement and control is estimated to be on the order of ±10 °C.

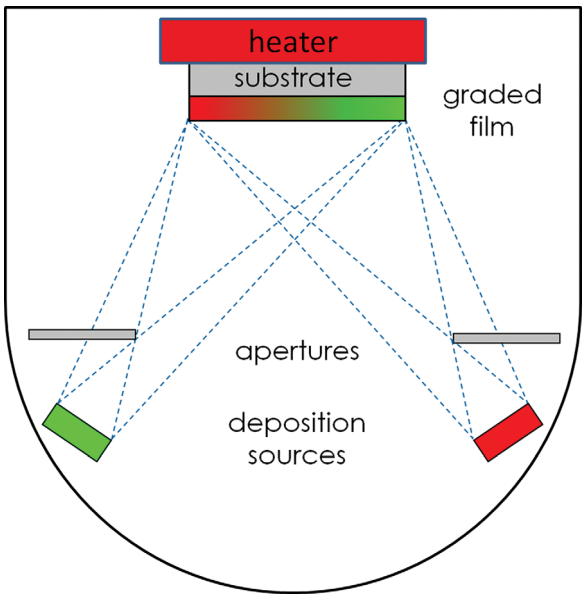

FIG. 1. Deposition system schematic showing the configuration for combinatorial coevaporation.

Film compositions were measured with a MAXXI-5 XRF spectrometer with a tungsten anode, operated with an acceleration voltage of 45 kV, and anode current of 700 μA. Elemental standards were used to determine XRF sensitivity factors for Cu, Zn, and Sn, and calibration runs were performed to characterize a background Sn signal related to the Mo/SLG substrate. This background signal was incorporated into the XRF data-analysis model to prevent over-estimation of Sn. While the statistical uncertainties from XRF data analysis were typically on the order of ±0.5%-1.0%, we conservatively estimate net uncertainties of ±3%. This value is more consistent with scatter observed in XRF mapping data sets, and accounts for ambiguities associated with subtraction of the Sn background signal. A Bruker AXS D8 Discover XRD instrument equipped with Hi-Star area detector was used to characterize crystalline-phase composition in the films. Raman spectroscopy measurements were performed with a Renishaw inVia Raman spectrometer. The excitation-laser wavelength was 532-nm, and samples were mapped on a 1-mm x-y grid. A Nova Nano630 SEM was used to characterize the plan view and cross-sectional film morphologies.

For photoluminescence (PL) imaging, 632.8-nm laser excitation ($\sim$70 mW/cm^2) was used. Photon emission was monitored with a Si charge-coupled device (CCD) detector. A long-pass filter (RG1000, transmission cutoff $\sim$1000 nm) was used to block reflected or scattered light from the excitation source. For spectral PL measurements, samples were excited with 1-mW (single-point measurements) and 5-mW (mapping measurements) 632.8-nm lasers, and PL spectra were collected with Si CCD array detectors coupled to Newport MS-260i spectrographs. In some of PL measurements, light was collected with a fiber optic that produced an absorption feature at $\sim$1.3 eV due to an OH vibrational mode. These absorption artifacts were corrected by normalizing PL spectra with respect to the OH absorption feature.

Qualitative electrical resistivity trends were estimated by measuring electrical resistance through film stacks, with tungsten electrodes contacting both the Mo layer on glass and various points on the front surface of the CZTS films.

III. RESULTS AND DISCUSSION

A. Results for 325 °C film growth temperature

Visual examination of the graded-composition Cu-Zn-Sn-S films grown for this study revealed obvious color and morphology variations. As shown by the photographic image in Fig. 2(a), both the Cu-rich and the Sn-rich sides of the film are somewhat rough. Also, although it is not obvious in the photograph, the Cu-rich side appears to the eye a gray-blue color, whereas the Sn-rich region is orange-brown. Between these two regions is a visually highly specular region that runs across the sample. These visual observations provide the first clues related to the effects of film composition on film crystalline phase content and morphology.

XRF measurements performed at the four corners and along the observed specular feature (1 mm/step) are summarized in Fig. 2(b). The film covers a wide compositional range in the phase diagram, and the directions of the Cu-, Zn-, and Sn-compositional gradients are consistent with the combinatorial-aperture and source orientations in the growth chamber. Results from an XRF line scan performed along the specular feature are plotted in the Cu_2S-ZnS-SnS_2 quasi-ternary composition space in Fig. 2(b). The measured compositions of the specular feature fall on a straight line in the ternary phase diagram that coincides with the ZnS-CZTS-CTS tie line. Compositionally, this line is characterized by the ratio $Cu/Sn = 2$.

Bragg-Brentano XRD measurements were performed to identify crystalline phases at various locations on the substrate. For these measurements, the sample was oriented with the x-ray plane of incidence parallel to the specular feature on the sample: in this orientation, elliptical areas probed by the x-ray beam are roughly aligned with the specular feature. It is well known that CZTS, ZnS, and CTS have very similar tetrahedrally coordinated crystal structures and lattice constants, and have overlapping peaks in conventional XRD analyses. Therefore, it is not surprising that all of the peaks observed in Fig. 3(a), acquired at points along the specular feature labeled A1-A5, can be explained by the presence of some combination CZTS, ZnS, and CTS. The strong peak at 26.7° in these spectra indicates that the CZTS exhibits preferential [112] texture. The data in Fig. 3(b) were acquired at points along a line roughly orthogonal to the direction of the specular feature, labeled B1–B7. XRD spectra acquired from the Cu-rich region (points B1–B3) show peaks that can be attributed to CZTS, ZnS, and/or CTS.[20] Additional peaks appear at 31.8°, corresponding to the (103) peak of the covellite CuS phase (PDF #98-000-0176), and at 46.1°, corresponding to the chalcocite Cu_2S (110) peak (PDF #98-000-0155). In some samples grown under similar conditions (not shown), the only Cu-S phase peaks that were observed in the Cu-rich regions belonged to covellite CuS. Based on these observations, we believe that CuS and/or Cu_2S can form as secondary phases in Cu-rich films (i.e., $Cu/Sn > 2$) depending on the sulfur flux and overall growth rate. The copper-sulfide peak intensities gradually decrease as Cu/Sn approaches 2, and drops below detection level on the specular feature. As the Cu/Sn ratio continues to decrease to values less than 2 in the Sn-rich region (point B5–B7), a distinct peak emerges at 50.0°, which is assigned to the (110) peak of the berndtite SnS_2 phase (PDF #98-000-0113). Neither Cu_xS nor SnS_2 peaks were observed along the specular feature. Indeed, there is no obvious change in the XRD spectra as Zn content varies along this feature, indicating as expected that XRD measurements cannot reliably differentiate between CZTS, ZnS, and CTS.

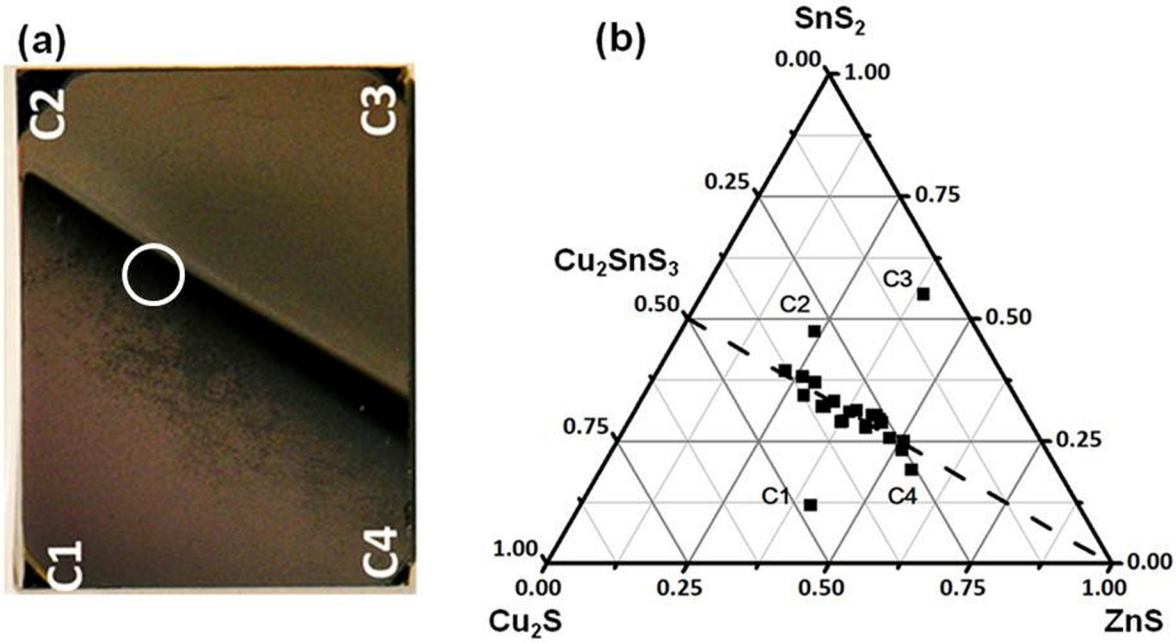

FIG. 2. (a) Optical image of a typical combinatorial CZTS thin film sample grown at 325 °C. Compared to the dark feature running diagonally across the sample (where $Cu/Sn \sim 2$), film roughness is higher in the Cu- and Sn-rich regions (near C1 and C3, respectively), and these areas are brighter in the photograph due to diffuse light scattering. (b) XRF compositional data from the four corners and along the specular feature, plotted in the Cu_2S-ZnS-SnS_2 quasi-ternary composition space. The white circle in (a) represents the approximate location of nominally stoichiometric CZTS.

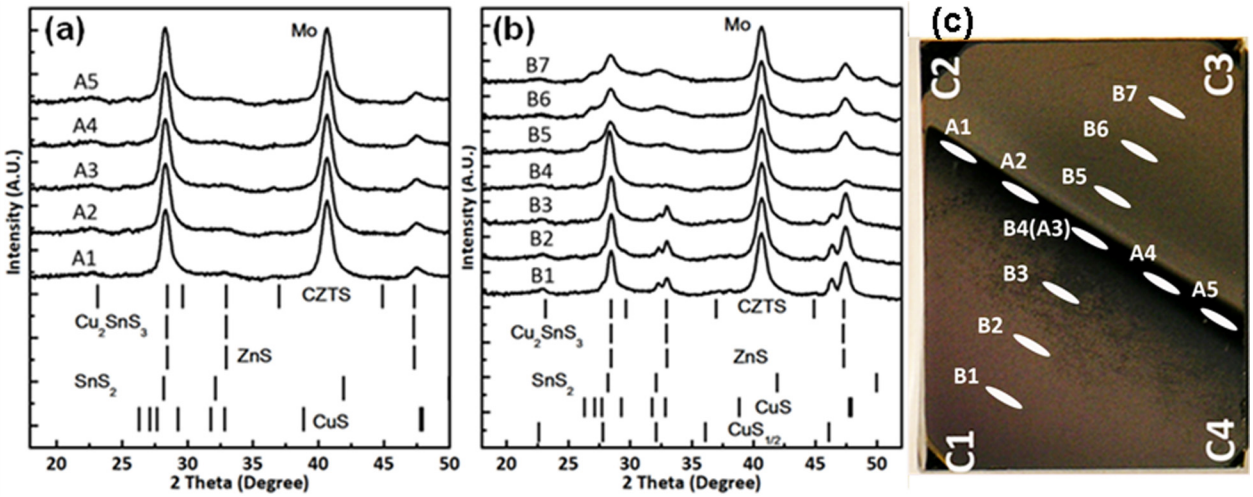

FIG. 3. XRD data sets acquired from the sample represented in Fig. 2. XRD measurements were performed on areas along the specular feature, marked as A1 to A5 (a), and along a line orthogonal to the specular feature, marked as B1 to B7 (b), as indicated in the photographic image (c). Areas labeled A1–A5 correspond to points spanning the specular feature, where film compositions are characterized by Cu/Sn ~ 2, with varying Zn content. Areas labeled B1–B7 correspond to measurements along the line connecting C1 and C3 on the graded sample.

Raman spectroscopy x-y mapping measurements on the combinatorial CZTS thin-film sample were performed on a 15×15 grid. Figures 4(a) and 4(b), respectively, show the intensity distributions of the 318 cm^{-1} (SnS_2) and 475 cm^{-1} (Cu_2S) peaks.[20–22] These intensity maps are consistent with the XRD results that detected Cu_xS phases in the Cu-rich region, and SnS_2 in Sn-rich region. A Raman peak at 370 cm^{-1} was used to map CZTS [Fig. 4(c)], because there is less overlap at this peak position with secondary-phase peaks than at 338 cm^{-1}, the main peak for CZTS.[20,23] It can be seen that the CZTS phase is relatively more concentrated close to the specular feature, where Cu/Sn = 2, and generally increases with increasing Zn content.

SEM was used to characterize film morphology. Panels (a), (b), and (c) in Figure 5 show the plan view surface morphologies of the Cu-rich, specular, and Sn-rich regions, respectively, and panels (d), (e), and (f) show the corresponding cross-sectional morphologies. Both Figs. 5(a) and 5(d) show that the Cu-rich region contains large grains embedded in a matrix of columnar dense small grains. Energy dispersive x-ray spectroscopy (EDX) and scanning Auger electron spectroscopy (AES) measurements (not shown) indicate that these large grains can be attributed to Cu_xS secondary phases. Moving from the most Cu-rich region on the sample toward areas with Cu/Sn ~ 2, the areal density of Cu_xS grains gradually decreases and eventually drops to zero in the specular region. Figs. 5(b) and 5(e) demonstrate that the film in the specular region, where Cu/Sn ~ 2, is smooth and lacks any clear signs of Cu_xS grains. The cross-sectional image indicates that the film is composed of small columnar grains, consistent with the XRD results that the film is strongly [112] textured. Moving toward Sn-rich (Cu/Sn < 2) film compositions, there is an abrupt change in morphology. As shown in Figs. 5(c) and 5(f), the top of the film becomes quite porous, and the top-most part of the film is composed of flake-like grains. Below the layer of flake-like grains, there is a dense film layer on the Mo/SLG substrate that is believed to be CZTS. The porous layer is consistent with SnS_2 phase observed in XRD. Atomic force microscopy (AFM) data acquired on these films (not shown) give values for root mean square (RMS) roughness of 155 nm for Cu-rich region, 7 nm for the specular region, and 56 nm for the Sn-rich region for scan area of 5 $\mu m \times 5$ μm. From the cross-sectional SEM images, it is clear that the film in the specular region is smooth and dense, with no evidence of voids. This morphology appears to be favorable for PV

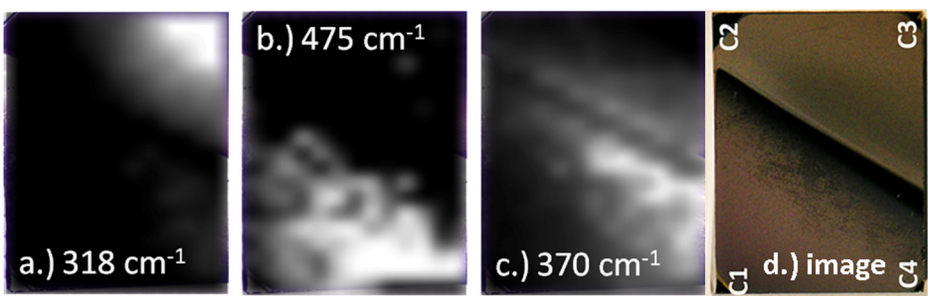

FIG. 4. Raman spectroscopic mapping data from the combinatorial CZTS sample shown in Fig. 2. Intensity maps are shown for (a) 318 cm^{-1}, corresponding to SnS_2, (b) 475 cm^{-1}, corresponding to Cu_2S, and (c) 370 cm^{-1}, corresponding to CZTS. For reference, the optical image is given in (d). Higher intensities in the maps represent more intense features in the Raman spectra, and are associated with higher mole fractions of the corresponding phases. The darker line in (c) overlaps with the specular feature for this sample, and is believed to be an artifact that results from enhanced reflection of the excitation light.

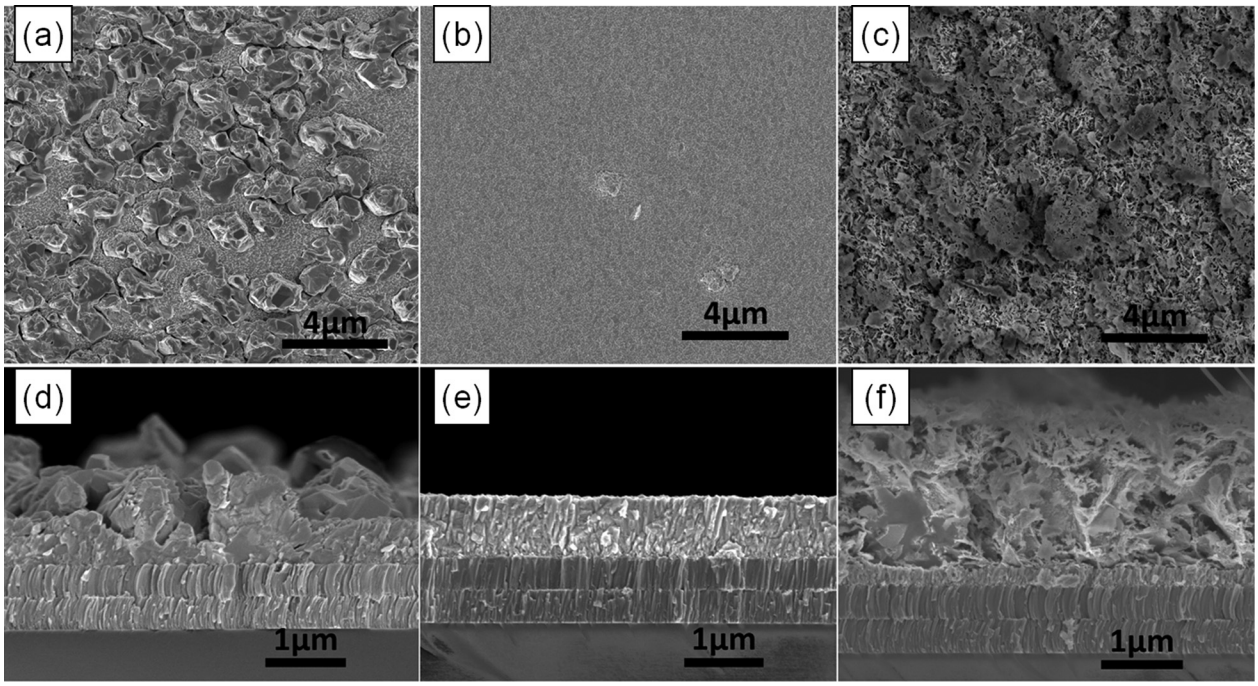

FIG. 5. Plan view and cross-sectional SEM images of the Cu-rich [(a) and (d)], specular [(b) and (e)], and Sn-rich [(c) and (f)] regions, respectively, of a combinatorial thin-film CZTS sample. The SEM data from the Cu-rich region [(a) and (d)] are representative of samples with compositions near C1 in Fig. 2(b), where Cu_2S is a dominant secondary phase. The specular region [(b) and (e)] is typical of samples with compositions that fall on the ZnS-CZTS-CTS tie line, where Cu/Sn $\sim$ 2. The Sn-rich SEM images are representative of samples with compositions similar to C3 in Fig. 2(b), for which SnS_2 is the dominant secondary phase.

applications, especially in comparison to the Cu-rich and Sn-rich regions. Additionally, film resistance measurements have shown that the Cu-rich region is highly electrically conductive, evidently because of the prevalence of highly conductive Cu_2S, a factor that would also be expected to negatively impact PV device performance.

Based on the XRF, XRD, Raman spectroscopy, and SEM results, a schematic thin-film quasi-ternary Cu_2S-ZnS-SnS_2 phase diagram is constructed, and illustrated in Fig. 6. The phases observed in the thin-film samples examined in this study are CZTS, CTS, Cu_2S, CuS, SnS, SnS_2, and ZnS. Phases such as Cu_3SnS_4 have been observed occasionally in Raman spectroscopy.[24] This phase, and the Cu_4SnS_4, $Cu_2Sn_4S_9$, and $Cu_2ZnSn_3S_8$ phases mentioned in the study of the bulk Cu_2S-ZnS-SnS_2 quasi-ternary phase system by Olekseyuk *et al.*[14] are not considered here, due to the fact that all of the XRD peaks observed in the present study can be assigned to other phases.

Our observation that the specular features in the combinatorial samples prepared in this study are coincident with the ZnS-CZTS-CTS tie line can be explained by the structural similarities between the ZnS, CZTS, and CTS crystalline phases. These three crystalline phases are all based on the zinc-blende crystal structure, in which each sulfur atom is tetrahedrally coordinated to four nearest-neighbor cations, and each cation is tetrahedrally coordinated with four sulfur

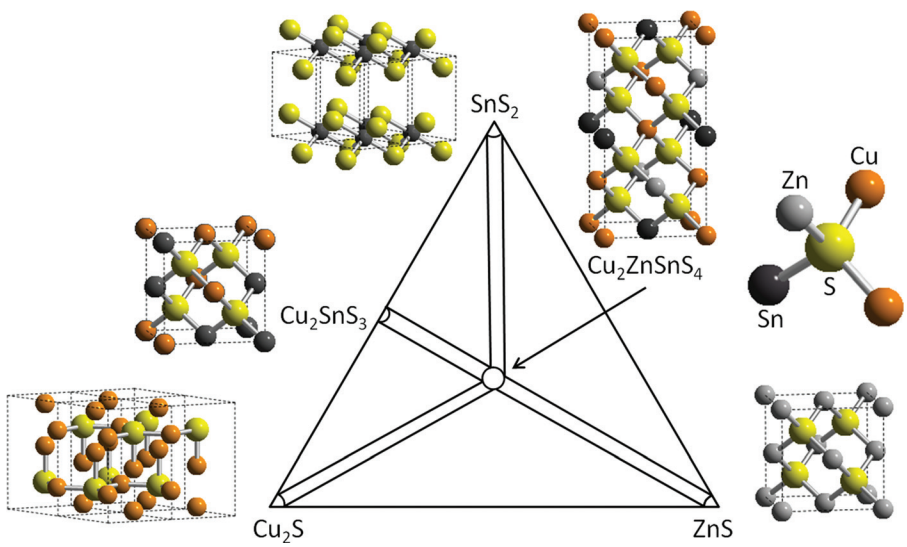

FIG. 6. Schematic of the thin film Cu_2S-ZnS-SnS_2 ternary phase diagram at 325 °C deposition temperature. The crystal structures of CZTS and the observed secondary phases are also presented, with unit cells represented by dashed lines. In the schematic of Cu_2SnS_3, the cation sublattice is randomized with respect to Cu and Sn occupancy.

atoms. Additionally, the lattice constants for ZnS, CZTS, and Cu_2SnS_3 are similar: the ZnS lattice constant is 5.41 Å, and those for CZTS and Cu_2SnS_3 are nearly identical at 5.43 Å.[14,24,25] The other secondary phases that have been observed have very different crystal structures, and this dissimilarity in crystalline structure leads directly to the observed effects on morphology.

B. Results for 475 °C film growth temperature

The films grown at 325 °C generally displayed poor opto-electronic properties, typified by very weak or non-existent photoluminescence response. We attribute this to poor crystalline quality associated with small grain sizes and high concentrations of extended and native point defects. Therefore, to better understand the effects of compositional variations on native defects in films with larger grains and higher degrees of crystalline quality, additional films were grown at 475 °C via combinatorial coevaporation. These high-temperature-processed samples generally showed robust room-temperature PL responses. They did not demonstrate as clear variations in color and film morphology as were observed in the lower-temperature samples. Nevertheless, some variations were observed between the Cu-rich (Cu/Sn > 2) areas versus regions falling on the ZnS-CZTS-CTS tie line: Cu-rich regions tended to exhibit a bluish hue and rough morphology, whereas regions with Cu/Sn ~ 2 were grayish and more specular.

PL-imaging and XRF measurements on a typical sample are shown in Fig. 7. In the PL image [Fig. 7(a)], bright areas with relatively high PL intensity correspond to the Cu-rich region. In addition, in the Cu-rich region, PL intensity increases with increasing Zn concentration, roughly from the midpoint between C1 and C2, diagonally toward C4. The highest PL intensity is toward the most Zn-rich region of the film, and near the bright-dark transition between the Cu-rich region and the region with Cu/Sn ~ 2. Film compositions mapped via XRF on a 5 × 5 grid are plotted in the ternary diagram in Fig. 7(b). XRF measurements were also performed along a line marking the boundary between high and low PL intensity regions [dotted line in Fig. 7(a)], and plotted in Fig. 7(c). An XRF-derived composition map of a typical sample grown at 325 °C is presented for comparison in Fig. 7(d).

For the film grown at 325 °C shown in Fig. 7(d), film compositions are distributed roughly uniformly on both sides of the line representing Cu/Sn = 2 ratio, which corresponds to the CTS–CZTS–ZnS tie line. For the sample grown at 475 °C, compositions in the Cu-rich region are distributed similarly to those of the 325 °C sample. On the other hand, film compositions in regions of the 475 °C sample that received excess Sn flux during growth have collapsed to the CTS–CZTS–ZnS tie line. This can be explained by the high vapor pressures of SnS_2 and SnS. At the growth temperature of 475 °C, only the required amount of Sn reacts with available Cu, Zn, and S to form CZTS; excess Sn is rejected due to the high vapor pressures of the Sn-S phases. In spite of the lack of measureable effects on composition, the intensity variations in the PL image show that excess Sn flux during growth can have important effects on the opto-electronic properties of coevaporated CZTS. These effects are discussed in more detail below.

Figure 8 shows XRD patterns acquired at different locations on the sample. Areas marked S1, S2, S3 are in the

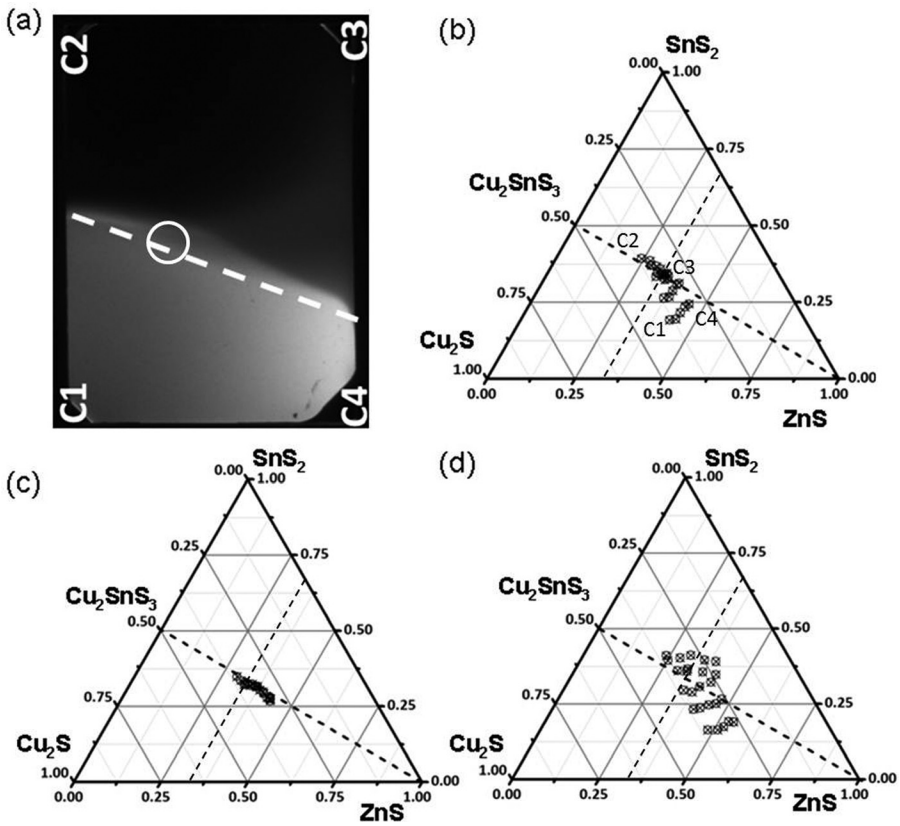

FIG. 7. (a) PL image of a combinatorially graded CZTS film grown at 475 °C. (b) Ternary compositions mapped by XRF measurements on a 5 × 5 grid with a spacing of 3–4 mm. (c) XRF compositions measured along the dashed line in the PL image [panel (a)]. (d) Ternary composition distribution of a typical sample grown at 325 °C. Comparison of panels (b) and (d) reveals that, in the high-temperature growth case, film compositions are observed only in regions of the quasi-ternary phase diagram where Cu/Sn ≥ 2, because Sn-S secondary phases are too volatile to condense under these growth conditions. The white circle in (a) represents the approximate position of nominally stoichiometric CZTS. In (b)–(d), the dashed lines representing Cu/Sn = Cu/Zn = 2 intersect at the nominally stoichiometric CZTS.

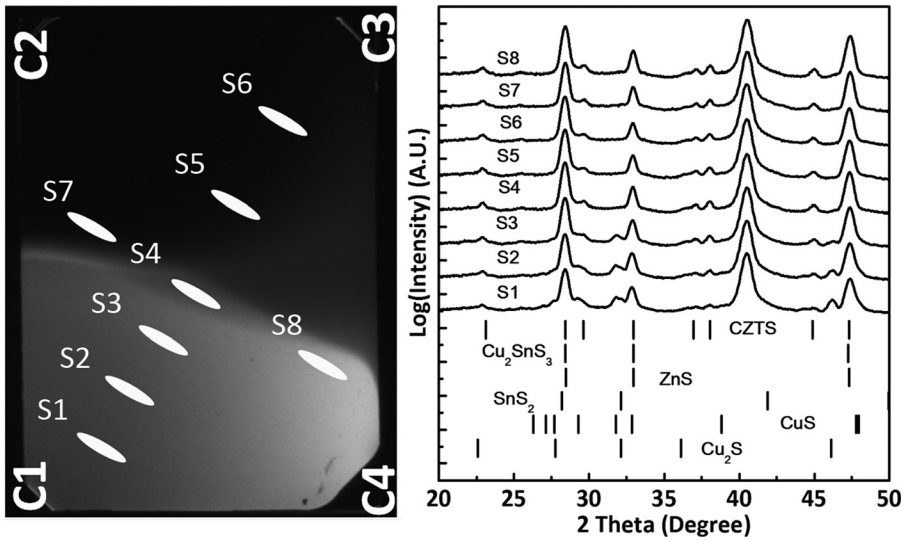

FIG. 8. PL image and XRD patterns from different locations on a combinatorially graded CZTS film grown at 475 °C. Film compositions are mapped in Fig. 7(b).

Cu-rich region, and for these XRD spectra CuS and Cu_2S peaks are observed at two-theta positions of 32.15° and 46.1°, respectively. These peaks decrease and eventually disappear near the transition between the bright and dark PL regions. On the bright/dark PL transition line and deep into the region that received excess Sn flux during film growth (S4–S8 in Fig. 8), the XRD patterns show no evidence of Cu_2S, CuS, SnS, or SnS_2 phases, consistent with the XRF data showing that compositions in the Sn-rich region collapse to the CTS–CZTS–ZnS tie line. In contrast, clear SnS_2 phases were observed in the Sn-rich region of samples grown at 325 °C. Because CTS, CZTS, and ZnS have similar crystal structures and lattice constants, XRD generally cannot distinguish between these phases. A detailed Raman spectroscopic analysis of similar samples focused on differentiating between these competing phases is presented in the accompanying study by Lund *et al.*[26]

Cross-sectional SEM was used to characterize morphology of films grown at 475 °C. Fig. 9(a) shows the morphology of the Cu-rich region. Large grains with voids throughout the film thickness were observed. XRD measurements (Fig. 8) and mapping AES measurements (not shown) show clear evidence of Cu-S secondary phases in films grown under Cu-rich conditions. The observed Cu-rich growth mode likely leads to shunting effects in completed PV devices. In addition, electrical resistance measurements showed that the Cu-rich region is highly conductive. This is believed to be either due to Cu-S metallic phases or p+ doping via Cu-related native point defects in the CZTS. Fig. 9(b) shows a cross-sectional SEM image of a Zn-rich region close to the tie line (close to S7 in Fig. 8). In this SEM image, bright grains with high secondary electron yields are observed. These bright areas have been identified as ZnS using EDX analysis (not shown). Scanning AES measurements on similar samples processed under Zn-rich conditions have also indicated the presence of ZnS. Fig. 9(c) shows a cross-sectional SEM image of a Sn-rich region of the film (similar to S5 in Fig. 8). Only a few very small ZnS grains in the CZTS-substrate interface are observed. The film is dense and shows columnar grain structure, consistent with the XRD finding that the film is textured.

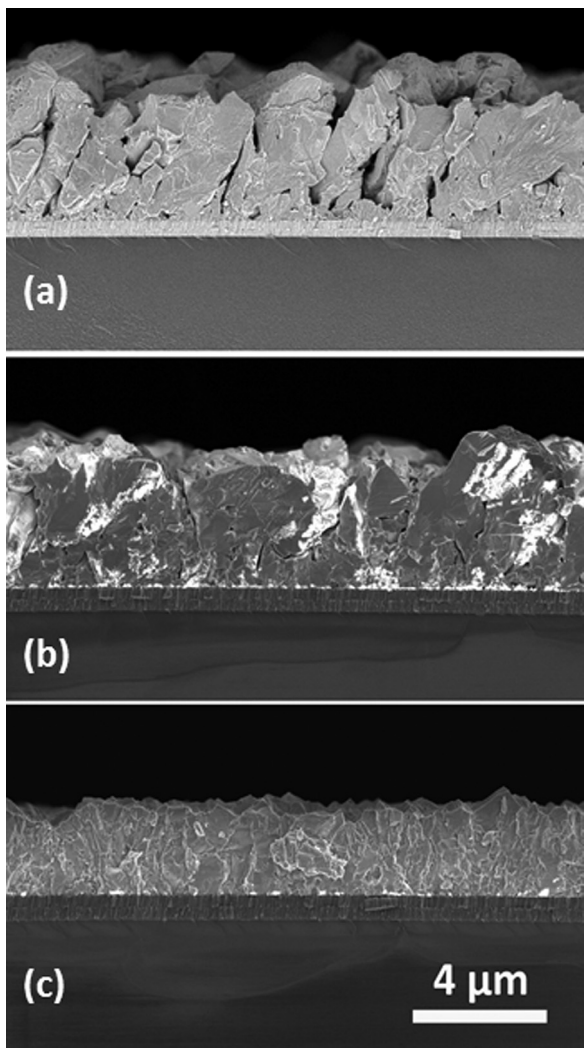

FIG. 9. Cross-sectional SEM images from typical CZTS films grown at 475 °C under varying conditions, including (a) Cu-rich (representative of area S2, Fig. 8), (b) Zn-rich (representative of area S8, Fig. 8), and (c) Sn-rich (representative of area S5, Fig. 8). In Cu-rich films, it is generally observed that film morphology is disrupted by the presence of secondary-phase Cu_2S. For Zn-rich films, film morphology is improved, in spite of the presence of substantial amounts of ZnS, which appear as bright features in the SEM image. The morphology of the film processed under Sn-rich growth conditions is the best, because no Sn-S secondary phases can form under these conditions due to their volatility.

In the sample shown in Figs. 7 and 8, it is particularly striking that PL intensity drops abruptly in regions of the sample that received excess Sn flux during growth, even though no measurable amount of excess Sn was incorporated into the film. We speculate that this effect can be traced to Sn-related native CZTS point defects, such as Sn_{Cu} and Sn_{Zn} antisites, or possibly neutral defect complexes such as $(2Cu_{Zn} + Sn_{Zn})$.[15–17,27] To further probe the effects of excess Sn flux during growth on film properties, compositionally graded CZTS films were characterized by room-temperature mapping-PL measurements on a 0.5-mm grid. The films represented in Figs. 10 and 11 are Cu-rich/Zn-rich, and Cu-poor/Zn-rich, respectively, relative to the film shown in Figs. 7 and 8. As illustrated in Fig. 12, the PL-mapping measurements demonstrate clearly that excess Sn flux during growth leads to quenched PL intensity, accompanied by a small shift to lower energy (~40 meV) of the peak emission energy. Additionally, the maximum PL intensity always occurs in regions that are Zn-rich relative to stoichiometric CZTS, i.e., where $Cu/Zn < 2$. These results are consistent with the common observation that the best PV device performance correlates with CZTS compositions that are Zn rich and Cu poor.

Zn-rich CZTS compositions correspond to regions along the tie line between CZTS and ZnS. According to the Cu_2S-ZnS-SnS_2 phase equilibria study by Olekseyuk *et al.*, one expects CZTS-ZnS equilibrium phase separation for compositions along this tie line beyond a few mol. % excess ZnS.[14] However, non-equilibrium conditions during processing are in general unavoidable. The high temperatures that are commonly used in CZTS processing (~450–500 °C) appear to be required for high-quality, large-grained CZTS films, and under these conditions there is an entropic driving force that produces higher concentrations of native point defects than exist in equilibrium at ambient temperatures. This effect expands the CZTS single-phase region at high temperature. High-temperature CZTS processing under Zn-rich conditions is, therefore, expected to produce material with relatively high concentrations of native defects that are favored by high Zn chemical potentials. These might include Zn_{Cu} and Zn_{Sn} point defects, or, as theoretically predicted by Chen *et al.*, neutral defect complexes such as $(Zn_{Sn} + 2Zn_{Cu})$ and $(Zn_{Cu} + V_{Cu})$. All of these native defects and complexes are predicted to be relatively benign, in that they do not lead to excessive doping or deep-level states that act as recombination centers.[15,17] As a Zn-rich CZTS sample is cooled from the highest processing temperature, some defects will be annealed out through diffusive processes accompanied by ZnS precipitation. But in some intermediate temperature range, atomic mobilities will drop below a critical value, at which point native defect concentrations and crystalline-phase content will be effectively frozen.

As evidenced by the higher PL response seen in Zn-rich CZTS compositions in this study, our results are consistent with the general observation that Zn-rich CZTS produces the highest efficiency CZTS devices, and in addition generally

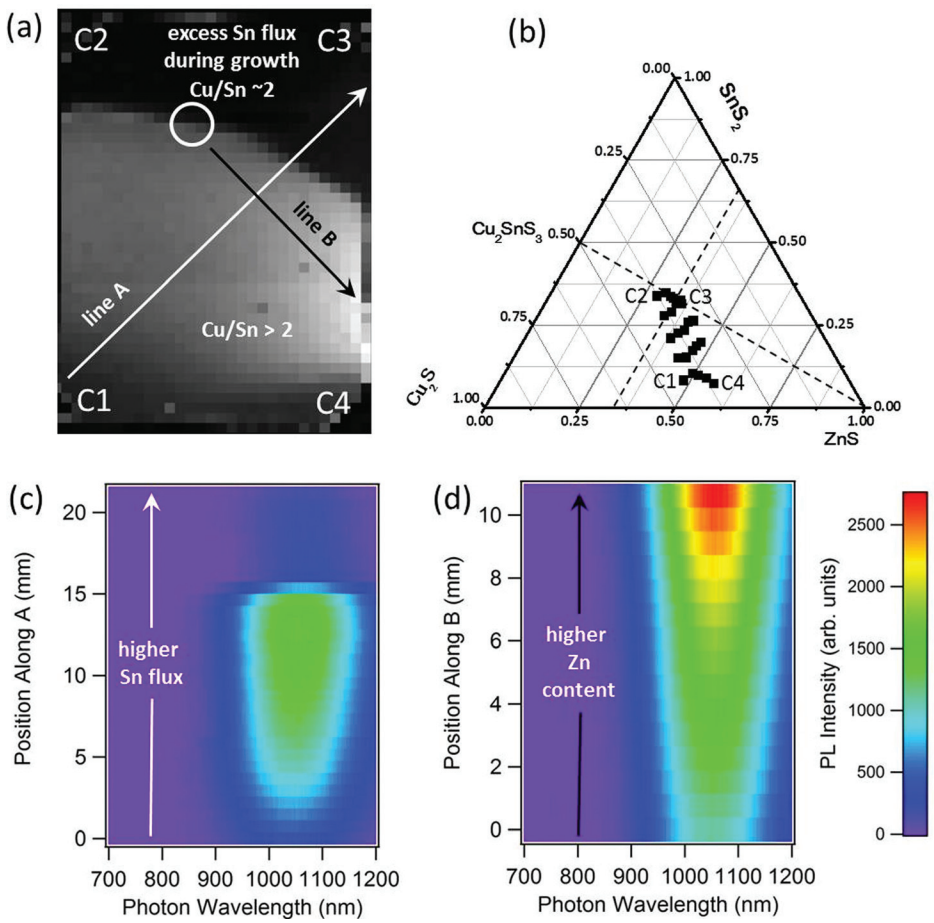

FIG. 10. (a) PL-mapping image at 1.35 eV (920 nm) of a compositionally graded CTZS film. The white circle represents the approximate position of nominally stoichiometric CZTS. (b) XRF measurements show that overall film composition is Cu and Zn rich. The dashed lines intersect at the nominal stoichiometry of CZTS. (c) PL profile along line A: moving from the most Cu-rich area (C1) toward the $Cu/Sn \sim 2$ line, the PL intensity increases steadily at first, then drops abruptly in areas that received excess Sn flux during growth. (d). PL profile along line B: intensity increases with increasing Zn content.

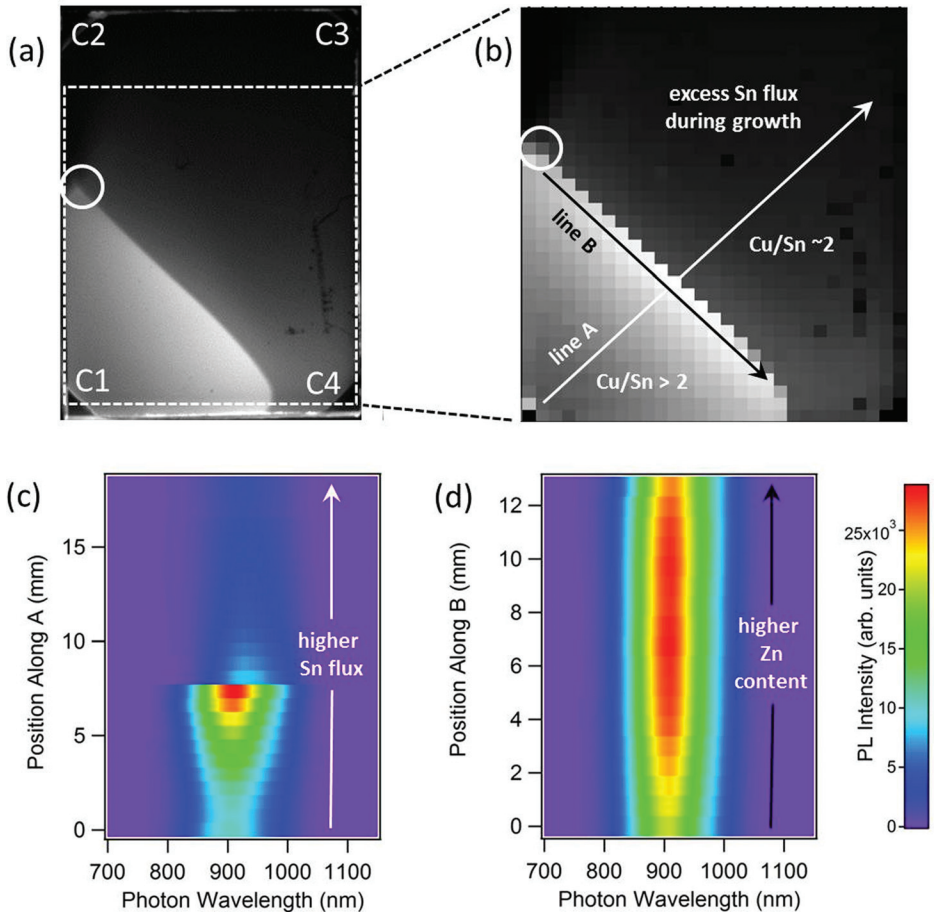

FIG. 11. (a) PL image and (b) PL-mapping image at 1.35 eV (920 nm) of a compositionally graded CTZS film. XRF data (not shown) indicate that the film is relatively Zn rich and Cu poor: the white circle in (a) and (b) represents the approximate position of nominally stoichiometric CZTS. (c) PL profile along line A: moving from the most Cu-rich area (C1) toward the Cu/Sn ~ 2 line, the PL intensity increases steadily at first, then drops abruptly in areas that received excess Sn flux during growth. (d) PL profile along line B: in the Zn-rich area of the film, PL intensity displays a shallow maximum with respect to overall Zn content.

support the theoretical point-defect models of Chen *et al*. On the other hand, the same theoretical models predict gradual variations in defect concentrations as a function of cation chemical potentials. In the case of Sn, the present study shows that there is an abrupt transition in opto-electronic properties that occurs at a critical Sn chemical potential. It remains to be seen whether this effect is compatible with existing theoretical models of defects in CZTS.

To further elucidate the effects of Sn chemical potential during growth and processing of CZTS, room-temperature PL spectra were acquired from a single compositionally uniform CZTS sample sequentially processed under four different conditions with respect to Sn flux, intended to mimic the final stages of film processing. Specifically, an individual CZTS sample was annealed under constant Sn and S fluxes at temperatures high enough (i.e., $>\sim 325\,^{\circ}C$) that Sn-S phases would not condense. During CZTS film growth or processing, the Sn chemical potential is determined by both substrate temperature and Sn flux. Therefore, by controlling these parameters, it is possible to shift the quasi-equilibrium

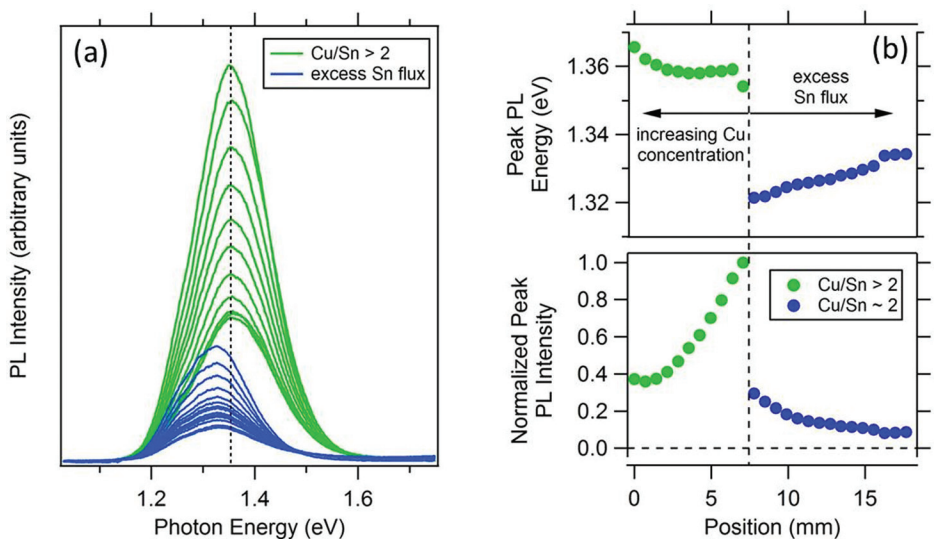

FIG. 12. (a) Twenty-six individual PL spectra along line A in Fig. 11(b). (b) Plots of normalized peak PL intensity and energy along the linescan.

CZTS point-defect concentrations toward or away from Sn-rich conditions. Very generally, less Sn, and therefore fewer harmful Sn-related antisite defects and complexes, are incorporated at higher annealing temperatures and/or at lower Sn fluxes. On the other hand, insufficient Sn flux leads to a Sn-deficient film and formation of Cu-S and ZnS secondary phases. Sn-related defects that might form under Sn-rich conditions include Sn_{Zn} and Sn_{Cu} point defects, and/or, as predicted by Chen *et al.*,[17] the defect complex $(2Cu_{Zn} + Sn_{Zn})$. All of these defects are predicted to lead to deep-level recombination centers, and are therefore expected to be harmful.

The results of the sequential processing series are illustrated in Fig. 13. Initially (after step #1), the PL emission is relatively strong, but processing at lower temperatures (steps #2 and #3) causes the PL emission spectrum to shift to lower energy and lower intensity. Lower substrate temperatures during the Sn-S anneal effectively increase the Sn chemical potential in the film. The system responds by incorporating more Sn, presumably in the form of native point defects and complexes. Processing step #4 returns the film to approximately its original condition, thereby demonstrating that the effect is reversible. Furthermore, elemental mobilities at these processing temperatures must be sufficiently high that chemical potential gradients in the film can be smoothed out on timescales on the order of minutes, typical of anneal times in these experiments. Overall, the sequential processing series results are entirely consistent with the PL mapping measurements described above, and together these results strongly support the hypothesis that Sn-related native point defects produce deep-level states that play an important role in non-radiative recombination processes.[15–17,27] While more detailed studies are needed to confirm this effect and elucidate the role of Sn-related native defects, it seems clear that the Sn chemical potential must be carefully controlled during CZTS film growth and processing.

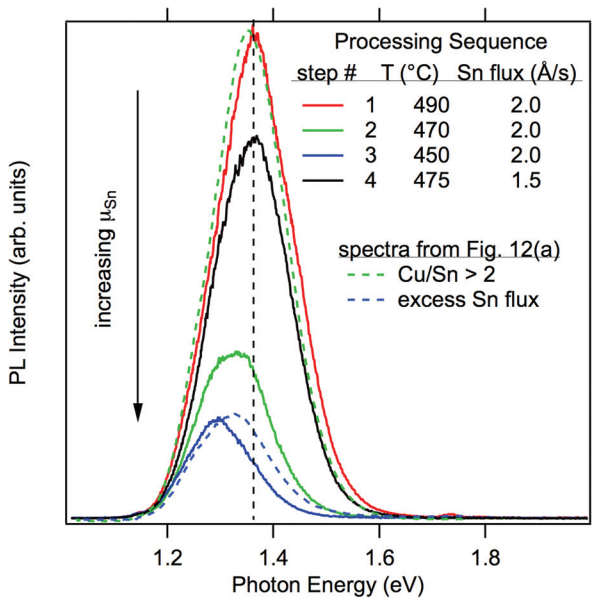

FIG. 13. Room-temperature PL spectra from a single CZTS sample sequentially processed under varying conditions with respect to Sn flux and annealing temperature. PL spectra were acquired subsequent to each process step. The PL spectrum shifts to lower peak energy and lower intensity under Sn-rich processing conditions (steps #2 and #3), and the effect is reversible when the film is processed under less Sn-rich conditions (step #4). The composition of the as-grown film was measured by XRF, and was slightly Zn-rich, with Cu/Sn ~ 2: (Cu, Zn, Sn) = (48.0%, 28.2%, 23.8%). Film composition was measured again after process step #2 and found to be (Cu, Zn, Sn) = (49.2%, 27.8%, 22.5%). These measurements are consistent to within the estimated error of the XRF measurement, about ±3%; therefore, it is concluded that film composition did not change significantly. Representative spectra from the Cu-rich and excess-Sn regions of the sample in Figs. 11 and 12.

IV. CONCLUSIONS

In this study, films were grown using combinatorial coevaporation methods at 325 °C and 475 °C. Film compositions were mapped using XRF, crystalline phases were identified using XRD and Raman spectroscopy, film morphology was characterized using SEM, and PL response was probed with a combination of room-temperature PL imaging, PL mapping, and single-point PL measurements. Based on these observations, and knowledge of the bulk quasi-ternary Cu_2S-ZnS-SnS_2 phase system, a schematic phase diagram for the thin-film CZTS system has been constructed. In the films grown at 325 °C, a specular region with compositions characterized by Cu/Sn ~ 2 coincides with the CTS–CZTS–ZnS tie line in the phase diagram. Cross-sectional SEM and XRD measurements demonstrate that films with Cu/Sn ~ 2 show a characteristic columnar-growth mode, and are strongly [112] textured. These features of the thin-film structure and morphology are a consequence of structural coherency that exists between the ZnS, CZTS, and CTS crystal structures. This structural coherency could have beneficial effects on PV device performance, because it could allow Zn-rich film compositions (with Cu/Sn ~ 2) that produce a favorable distribution of point-defect concentrations that optimize opto-electronic film properties, without leading to the formation of secondary phases that have detrimental effects on film morphology. In films grown at 475 °C, film compositions in regions that received excess Sn flux during growth collapsed to the CTS–CZTS–ZnS tie line as a result of the volatility of Sn-S phases. While film decomposition and Sn loss during high-temperature processing can be prevented by providing an excess Sn flux, PL measurements support the hypothesis that excess Sn can create high concentrations of Sn-related native point defects that limit minority-carrier lifetime and device performance.

ACKNOWLEDGMENTS

This work was supported by the U.S. Department of Energy under Contract No. DE-AC36-08GO28308 with the National Renewable Energy Laboratory.

[1]I. Repins, M. A. Contreras, B. Egaas, C. DeHart, J. Scharf, C. L. Perkins, B. To, and R. Noufi, Prog. Photovoltaics **16**, 235–239 (2008).
[2]P. Jackson, R. Würz, U. Rau, J. Mattheis, M. Kurth, T. Schlötzer, G. Bilger, and J. H. Werner, Prog. Photovoltaics **15**, 507–519 (2007).
[3]P. Jackson, D. Hariskos, E. Lotter, S. Paetel, R. Wuerz, R. Menner, W. Wischmann, and M. Powalla, Prog. Photovoltaics **19**, 894–897 (2011).
[4]X. Wu, J. Zhou, A. Duda, J. C. Keane, T. A. Gessert, Y. Yan, and R. Noufi, Prog. Photovoltaics **14**, 471–483 (2006).
[5]B. A. Andersson, Prog. Photovoltaics **8**, 61–76 (2000).

[6]T. K. Todorov, J. Tang, S. Bag, O. Gunawan, T. Gokmen, Y. Zhu, and D. B. Mitzi, Adv. Energy Mater. **3**, 34–38 (2013); M. T. Winkler, W. Wang, O. Gunawan, H. J. Hovel, T. K. Todorov, and D. B. Mitzi, Energy Environ. Sci. **7**, 1029 (2014).
[7]T. K. Todorov, K. B. Reuter, and D. B. Mitzi, Adv. Mater. **22**, E156–E159 (2010).
[8]K. Wang, O. Gunawan, T. Todorov, B. Shin, S. J. Chey, N. A. Bojarczuk, D. Mitzi, and S. Guha, Appl. Phys. Lett. **97**, 143508 (2010).
[9]Q. Guo, H. W. Hillhouse, and R. Agrawal, J. Am. Chem. Soc. **131**, 11672–11673 (2009).
[10]Q. Guo, G. M. Ford, W.-C. Yang, B. C. Walker, E. A. Stach, H. W. Hillhouse, and R. Agrawal, J. Am. Chem. Soc. **132**, 17384–17386 (2010).
[11]D. A. R. Barkhouse, O. Gunawan, T. Gokmen, T. K. Todorov, and D. B. Mitzi, Prog. Photovoltaics **20**, 6–11 (2012).
[12]B. Shin, O. Gunawan, Y. Zhu, N. A. Bojarczuk, S. J. Chey, and S. Guha, Prog. Photovoltaics **21**, 72–76 (2013).
[13]A. Nagoya, R. Asahi, R. Wahl, and G. Kresse, Phys. Rev. B **81**, 113202 (2010).
[14]I. D. Olekseyuk, I. V. Dudchak, and L. V. Piskach, J. Alloys Compd. **368**, 135–143 (2004).
[15]S. Chen, J. Yang, X. G. Gong, A. Walsh, and S. H. Wei, Phys. Rev. B **81**, 245204 (2010).
[16]K. Biswas, S. Lany, and A. Zunger, Appl. Phys. Lett. **96**, 201902 (2010).
[17]S. Chen, A. Walsh, X. G. Gong, and S. H. Wei, Adv. Mater. **25**, 1522–1539 (2013).
[18]W. J. Yin, Y. Wu, S. H. Wei, R. Noufi, M. M. Al-Jassim, and Y. Yan, Adv. Energy Mater. **4**, 1300712 (2014).
[19]X.-D. Xiang, Ann. Rev. Mater. Sci. **29**, 149–171 (1999).
[20]P. A. Fernandes, P. M. P. Salome, and A. F. da Cunha, Thin Solid Films **517**, 2519–2523 (2009).
[21]G. A. Hope, C. G. Munce, G. K. Parker, and S. A. Holt, Colloids Surf., A **295**, 152–158 (2007).
[22]L. S. Price, I. P. Parkin, T. G. Hibbert, and K. C. Molloy, Chem. Vap. Deposition **4**, 222–225 (1998).
[23]X. Fontane, L. Calvo-Barrio, V. Izquierdo-Roca, E. Saucedo, A. Perez-Rodriguez, J. R. Morante, D. M. Berg, P. J. Dale, and S. Siebentritt, Appl. Phys. Lett. **98**, 181905 (2011).
[24]P. A. Fernandes, P. M. P. Salome, and A. F. da Cunha, J. Phys. D **43**, 215403 (2010).
[25]J. C. Jamieson and H. H. Demarest, Jr., J. Phys. Chem. Solids **41**, 963–964 (1980).
[26]E. A. Lund, H. Du, W. M. Hlaing Oo, G. Teeter, and M. A. Scarpulla, J. Appl. Phys. **115**, 173503 (2014).
[27]M. J. Romero, H. Du, G. Teeter, Y. Yan, and M. M. Al-Jassim, Phys. Rev. B **84**, 165324 (2011).